PERGAMON

International Journal of Multiphase Flow 27 (2001) 1533–1554

International Journal of Multiphase Flow

www.elsevier.com/locate/ijmulflow

A study of drift velocity in bubbly two-phase flow under microgravity conditions

N.N. Clarke, K.S. Rezkallah *

Department of Mechanical Engineering, University of Saskatchewan, Saskatoon, Canada S7N 5A9

Received 26 June 2000; received in revised form 23 March 2001

Abstract

The results from a numerical simulation of microgravity bubbly gas–liquid two-phase flow are presented and compared against experimental data collected during parabolic flights on NASA's KC-135 aircraft. The simulation produced comparable results for the drift velocity and the rate at which bubbles move towards the center of the tube. The simulations were done for a range of parameters; including the liquid Reynolds number (1000–25,000), the bubble size relative to the tube diameter (0.1–0.3), surface tension (7.28×10^{-2}–2.18×10^{-1} N/m), and tube diameter (9.525–40 mm). The results showed excellent comparisons with the bubble shape and evolution, the magnitude of the drift velocity, and the distance that the bubble moves towards the tube center. It was concluded that the bubble diameter, radial bubble position, liquid Reynolds number, and tube diameter all have major influence on the drift velocity.

Keywords: Bubbly flow; Microgravity; Two-phase; Lift force

1. Introduction

The behavior of two-phase, gas–liquid mixtures has been extensively investigated during the past five decades. Recently, access to near weightlessness environment (known as "microgravity") has allowed researchers to study two-phase flows in the absence of gravity-induced buoyancy effects. The subject of this study is to utilize the microgravity environment in predicting the drift velocity in bubbly flow. This is of particular interest since many of the body forces acting on a bubble are small compared to buoyancy, and their effects are severely masked by buoyancy effects under normal gravity conditions.

* Corresponding author.
E-mail address: kamiel@engr.usask.ca (K.S. Rezkallah).

0301-9322/01/$ - see front matter
PII: S0301-9322(01)00027-1

One important aspect in predicting bubbly two-phase flow is to determine the void fraction distribution across the flow channel width. To illustrate the significant effect that gravity imposes on the radial gas void fraction distribution in a conduit, data for upward vertical flow (Serizawa et al., 1975), downward vertical flow (Wang et al., 1987), and microgravity (Kamp et al., 1993) are shown in Fig. 1. The plot gives the void fraction, ϵ, as a function of a dimensionless distance measured from the tube center (r/R). The l-g upward dispersed bubbly flow exhibits the typical "saddle" shape with the highest void fraction and bubble density concentration near the wall of the tube. The downward flow has a "square" distribution with the maximum bubble density farther away from the wall and then mostly flat along the remainder of the cross-section of the channel. The microgravity void distribution, on the other hand, shows a parabolic profile similar to that obtained in single-phase flows with a distinct maximum at the center of the channel.

In the past, bubbly flow modeling has centered around the two-fluid model of Ishii (1975), which is based on a time-averaging technique for both phases. Several researchers have used the two-fluid model to predict the radial void profile; e.g., Drew and Lahey (1982), and Antal et al. (1991). Most modeling efforts were limited to l-g flows, and very little work has been done for microgravity flows.

Among the very few efforts to model such flows at μ-g are those reported by Lahey and Bonetto (1994), and Singhal et al. (1996). In their experimental work they simulated microgravity by using neutrally buoyant particles (or oil) at very low void fractions (0.07–0.21%). The resultant bubble sizes (<400 μm) are not of practical application to the μ-g environment. In microgravity conditions, higher void fractions are usually encountered and the diameter of the spherical bubbles is in many cases larger than 50% of the tube diameter. More recently, Lin and Rezkallah (1995) developed a numerical two-fluid model to predict the void fraction distribution and turbulence

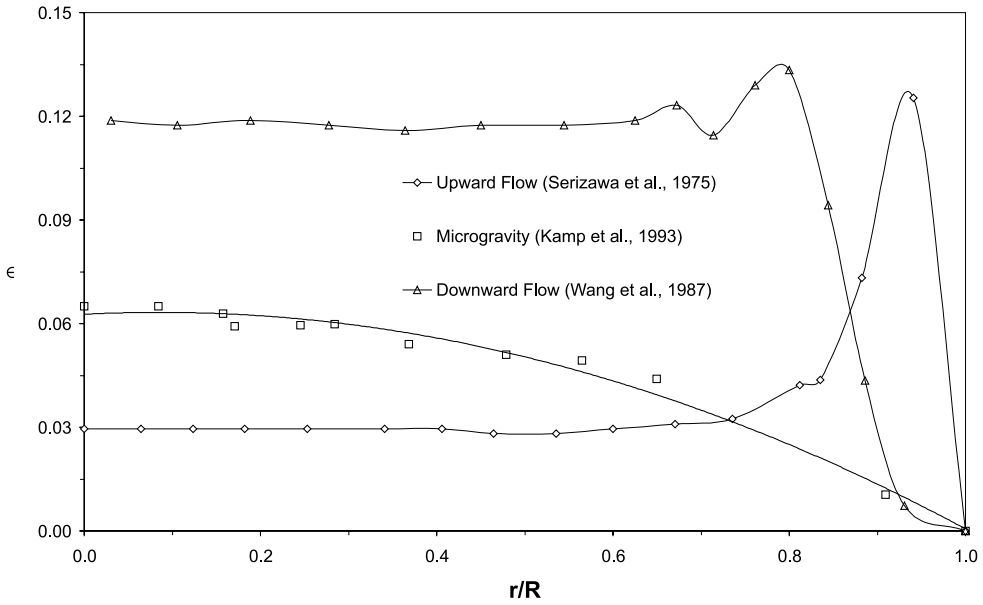

Fig. 1. Typical void fraction profiles for upward flow (Serizawa et al., 1975), downward flow (Wang et al., 1987), and microgravity flow (Kamp et al., 1993).

structure in bubbly flow under μ-g conditions. As part of their model, a drift velocity resulting from a lift force acting on the bubble was included as a major contributor to the development of the void fraction profile. The lift force is the net force acting radially upon a gas bubble moving through a liquid velocity field (non-stagnant). The lift force will move the bubble either towards the center of the pipe or close to its wall depending on the direction of the net force acting on the bubble.

Most lift force expressions, including the one used earlier by Lin and Rezkallah (1995), have been derived for the normal gravity condition. This limits their use in μ-g conditions due to the significant reduction in gravitational force, and hence the net forces acting on a bubble. The two most prevalent lift force models at l-g are those of Saffman (1965, 1968), and Drew and Lahey (1987). Their dependence on a interphase slip velocity (due to buoyancy) makes them inappropriate for microgravity where the slip velocity in bubbly flow approaches zero. The no-slip condition in μ-g bubbly flow was further studied and confirmed by Rezkallah and Nakazawa (1998), who also showed that outside the bubbly flow regime a positive slip ratio exists for other flow regimes, even at microgravity.

One expression that was derived for l-g data but could be applied to μ-g is that of Cox and Hsu (1977). In the model, the lift force was placed in the form of a drift velocity (V_{drift}), and was solved for a small neutrally buoyant bubble (which in our case simulates the microgravity condition). The drift velocity, V_{drift}, in the Cox and Hsu model is given by

$$V_{\text{drift}} = \frac{1}{144}\frac{a^3 U_0^2}{v_L R^2}\left(1 - \frac{R-r}{R}\right)\left(61 - 184\frac{R-r}{R}\right), \tag{1}$$

where a is the bubble radius, R is the tube radius, r is the distance from bubble to tube center, U_0 is the maximum liquid velocity, and v_L is the liquid kinematic viscosity.

The limitations of this model are due to the assumption of creeping liquid flow and it only applies to very small non-deformable bubbles (particle flows). Its inclusion in the model of Lin and Rezkallah (1995) shows the limitations of the current lift force and drift velocity modeling. The high liquid velocities and large bubbles of μ-g flows exhibit a different mechanism of motion; this is illustrated in Fig. 2. In that figure, the Lin and Rezkallah's model is compared to the μ-g experimental data of Kamp et al. (1993). The numerical model predicts a maximum void fraction away from the centerline in contrast to the clearly distinct maximum at the centerline of the experimental data. The drift velocity expression of Cox and Hsu (1977) predicts that bubbles near the wall would move towards the center and that bubbles near the center would move towards the wall, hence the maximum void fraction is somewhere in between. This also contradicts the μ-g experimental data. To improve upon the modeling of void fraction profiles in the microgravity case, the drift velocity model must be first improved.

One method that shows promise in providing a better understanding of drift velocity in microgravity is the interface tracking technique. Interface tracking methods have allowed researchers to simulate the motion of individual gas bubbles in a liquid flow using computational techniques. The volume of fluid (VOF) method proposed by Hirt and Nichols (1981) is one such technique used by Tomiyama et al. (1995) to examine several different problems including Taylor bubble shapes, the interaction of two bubbles rising in a stagnant liquid and the lateral migration of a two- dimensional bubble in a linear shear flow. The lateral migration of a two-dimensional bubble in liquid shear followed the expected behavior. For a large bubble, the bubble deformed

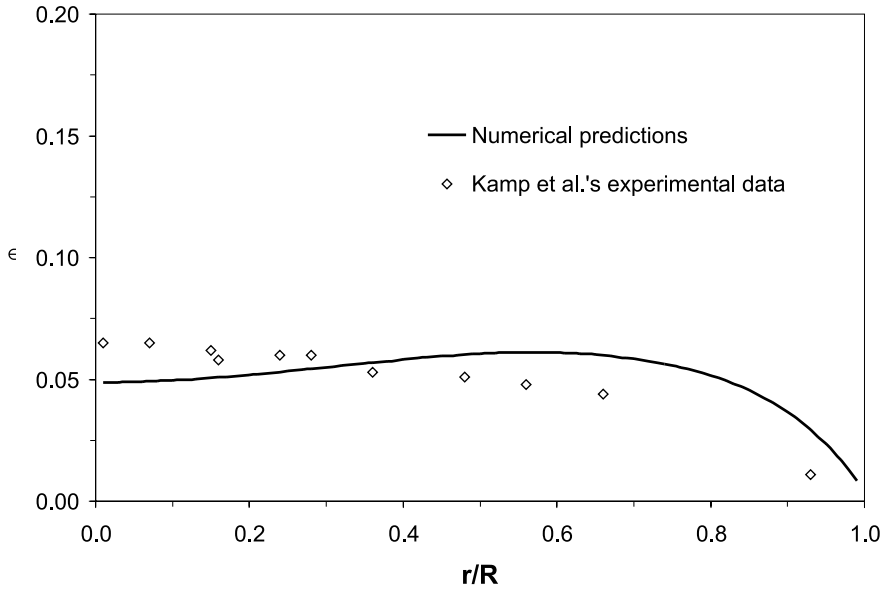

Fig. 2. Predicted and experimental void fraction profiles in μ-g flow (Lin and Rezkallah, 1995).

into a wing-shape and then proceeded to move to the region of higher velocity (coring) which reflects what has been previously observed for bubbles larger than 5 mm in diameter. For a small non-deformable bubble, the simulated bubble moved to the side of lower velocity reflecting the wall-peaking seen in the experimental studies. Beyond the two-dimensional bubble simulation, Tomiyama et al. (1995) extended the code to model three-dimensional bubbles as well.

By using a simulated bubble in microgravity conditions, the effect of various parameters could be observed by varying more parameters that could significantly affect the bubble motion and by observing the lateral motion of a single bubble within a liquid flow. Hence, a better understanding of the mechanism of drift velocity at microgravity can be attained.

2. Mechanism of drift velocity

The lift force and drift velocity forces are in fact two byproducts of the bubble drag in the constitutive relations of the two-fluid model. It is helpful to refer to Fig. 3 to become familiar with the geometry and forces involved in the lift force. When the hydrodynamic force on the bubble is estimated, there is a component of the force that is parallel to the flow direction. Perpendicular to this force is the lift force component responsible for the bubble drift velocity. Video images of microgravity two-phase flow regimes were collected in a series of experiments performed since 1988 by the Microgravity Research Group. The video sequences reported by Lowe and Rezkallah (1999) for water–air in a 9.525 mm tube clearly show the behavior of individual gas bubbles in microgravity. Using the Matrox Inspector software for PC computers, video images were digitized for image processing and analysis. Fig. 4 shows three typical images of bubbly flow at three superficial liquid velocities (V_{SL}), ranging from 0.74 to 2.53 m/s. Fig. 4(a) ($V_{SL} = 0.74$ m/s) shows

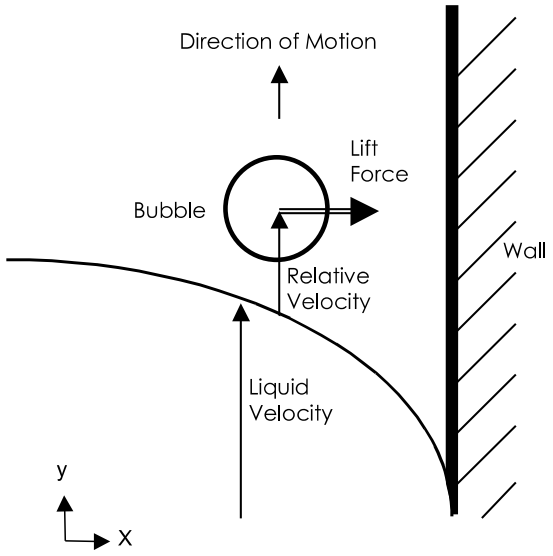

Fig. 3. Force balance on a bubble near a wall.

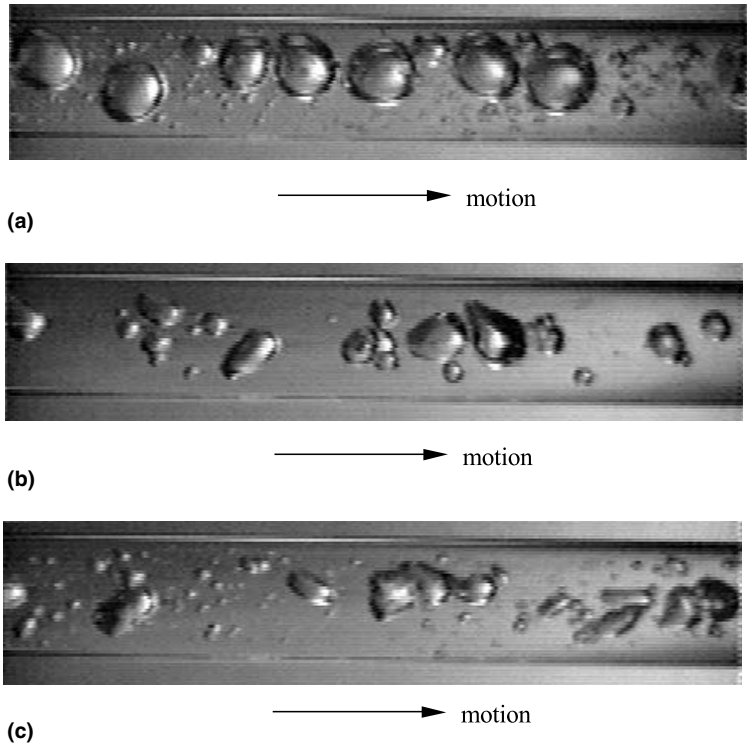

Fig. 4. Bubbly flow images at increasing liquid velocity in μ-g (air–water $D = 9.525$ mm); (a) $V_{SL} = 0.74$ m/s, $V_{SG} = 0.09$ m/s, (b) $V_{SL} = 1.72$ m/s, $V_{SG} = 0.074$ m/s, and (c) $V_{SL} = 2.53$ m/s, $V_{SG} = 0.067$ m/s.

mostly large, nearly spherical bubbles of diameters up to 5 mm (almost half the tube diameter), interspersed with small scattered bubbles. In contrast, Fig. 4(b) shows bubbles that are smaller in size and have become deformed and also elongated in shape. Such deformation is attributed to the increased liquid velocity, and hence the shear force acting on the bubbles. The deformation of the bubbles is even more obvious in Fig. 4(c) for the case of $V_{SL} = 2.53$ m/s. Significant elongation can be seen in the smaller bubbles while the larger bubbles are often deformed into erratic shapes due to the surrounding turbulent flow. The liquid shear acting upon the bubbles increases with increasing the Reynolds number, causing the bubbles to deform away from the spherical shape caused by surface tension forces acting on the bubbles. It should be noted that great care was taken that surface deformation due to optical path bending is minimized. This was accomplished by placing the acrylic test section tube inside a light path correction box (see Lowe and Rezkallah (1999) for more details).

Careful observation of the video sequences shows several examples of bubbles moving towards the center of the tube as they pass through the camera's field of view. Three examples of bubbles moving laterally within the viewing section (5 cm long) are shown in Fig. 5. Each image shows a single isolated bubble as it moves through the viewing section. The surrounding bubbles have been removed for clarity and the five separate bubble images have been combined into one single image for better comparison of shape and position within the tube as the bubble travels downstream. In Fig. 5(a), $V_{SL} = 0.74$ m/s, and while the bubble does not deform appreciably as it passes through the viewing section, the motion of the bubble towards the center is clearly seen. The bubble sequences for $V_{SL} = 1.72$ m/s, and $V_{SL} = 2.53$ m/s show progressively more bubble elongation and

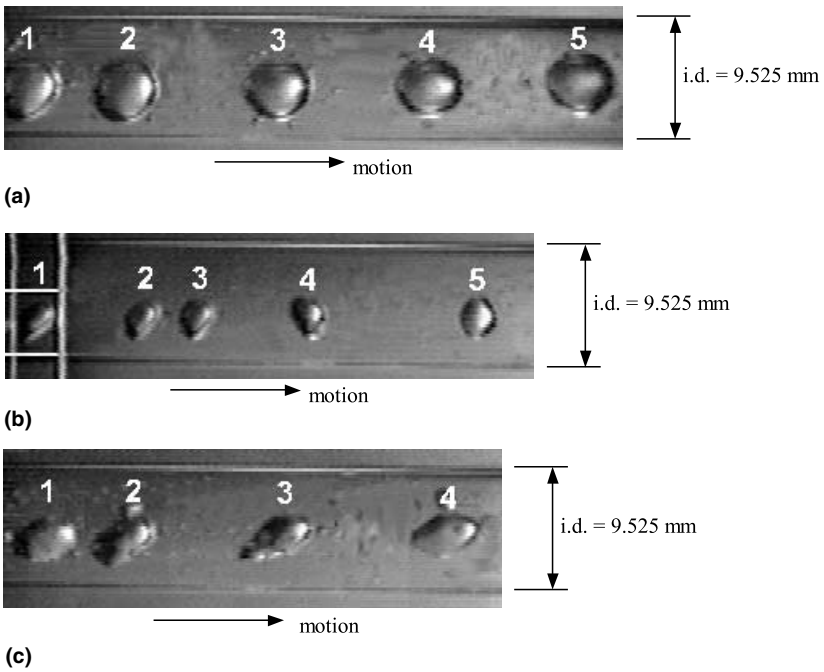

Fig. 5. Bubble sequences at increasing liquid velocity in μ-g (air–water $D = 9.525$ mm); (a) $V_{SL} = 0.74$ m/s, $V_{SG} = 0.09$ m/s, (b) $V_{SL} = 1.72$ m/s, $V_{SG} = 0.074$ m/s, and (c) $V_{SL} = 2.53$ m/s $V_{SG} = 0.067$ m/s.

radial motion with increasing the liquid velocity. It is interesting to observe that the bubbles return to a more spherical shape once they reach the core region of the tube. The wing-like elongation of the bubbles, shown in Figs. 5(b) and (c) would appear to be the result of a higher liquid shear around the bubbles. This aspect will be discussed later in some detail.

The mechanism of bubble motion in a turbulent liquid flow at microgravity conditions has not been previously investigated in the literature. The large deformable bubbles in microgravity two-phase flow are the source of difficulty in adequately modeling the lift force or drift velocity. Most previous work has approximated a bubble as a solid sphere. While this is reasonable for small bubbles, the tendency of large bubbles to deform adds another complexity to the problem of accurately predicting the drift velocity and the lift force. The motion of a large bubble is dependent upon its shape and the flow of liquid around the bubble surface. The shape of the bubble influences the liquid flow around it and vice versa. It is therefore necessary to consider effects such as the forces acting upon the surface of a bubble (through the boundary conditions which subsequently dictate the shape of the bubble), the flow of the liquid around the gas bubble and more specifically, to investigate the dynamics at the gas bubble/liquid interface.

The no-slip condition, usually assumed for μ-g bubbly flows, indicates that a bubble moving axially along the tube surface in a shear flow would experience a relative velocity in the upstream direction near the wall-side. At the tube center, the bubble would experience a downstream relative velocity. This shear force acting on the bubble would "stretch out" the bubble into what is seen as an ellipsoidal bubble.

The surface stress boundary condition at the interface is made up of two parts: tangential and normal stresses. The tangential stress on the interface is given by the following equation

$$\left[\mu\left(\frac{\partial U_n}{\partial s}+\frac{U_s}{\partial n}\right)\right]_1=\left[\mu\left(\frac{\partial U_n}{\partial s}+\frac{\partial U_s}{\partial n}\right)\right]_2+\frac{\partial\sigma}{\partial s}, \tag{2}$$

where s refers to the tangential direction, n to the normal direction, U is the liquid velocity, and the subscripts 1 and 2 refer to phases 1 and 2, respectively. The normal stress is given by

$$\left(P-2\mu\frac{\partial U_n}{\partial n}\right)_1=\left(P-2\mu\frac{\partial U_n}{\partial n}\right)_2-\sigma\kappa, \tag{3}$$

where P is the pressure, μ is the viscosity and κ is the curvature of the interface.

If the change in surface tension along the surface is assumed to be negligible (because of the absence of a temperature gradient or surface contamination), the tangential stress equation represents a balance between the viscous forces on each side of the interface. The liquid flow around the bubble surface stretches it into a wing-shape as seen in Figs. 5(b) and (c), where the surface tension has been "overpowered" by the high liquid shear. Conversely at lower liquid flow rates the surface tension is the dominant force and spherical bubbles, such as the one shown in Fig. 5(a), are observed. The bubble elongation caused by the forces acting on the bubble interface appears to be a major contributor to the lateral motion of the bubble towards the tube center. This also will be discussed later in some detail.

Reviewing the interface boundary conditions, it can be stated that the bubble shape and drift velocity are influenced by the liquid velocity, fluid viscosity, and surface tension. Also, the bubble size must have some effect on the drift velocity. The latter will affect the shape of the bubble in that the radius of the interface curvature changes with bubble size. The liquid shear surrounding the

bubble is dependent upon the location of the bubble with respect to the tube wall, especially in turbulent flows. In turbulent flows, high velocity gradients exist near the walls and are reduced towards the center of the tube. Thus, the bubble position will also be a significant factor in the prediction of the drift velocity.

3. Analysis

3.1. Dimensional analysis

Assuming that no mass or heat transfer occurs across the bubble interface, inertial and viscous forces within the gas bubble are negligible, constant surface tension, the drift velocity of a single bubble in a moving liquid flow within a cylindrical tube is a function of the following flow parameters and liquid-phase properties:

$$V_{\text{drift}} = f(U, d, s, D, \rho_{\text{L}}, \mu_{\text{L}}, \sigma). \tag{4}$$

A dimensional analysis was performed on the dependent parameters and the result was the following dimensionless groups: dimensionless drift velocity (V^+), a dimensionless distance from the wall (β), a dimensionless bubble diameter (γ), the liquid Reynolds number (Re), and the liquid Weber number (We). The parameters and dimensionless groups are summarized in Table 1. The dimensional analysis yields a dimensionless bubble drift velocity as a function of the following dimensionless variables:

$$V^+ = f(\beta, \gamma, Re, We). \tag{5}$$

3.2. Test matrix

A test matrix was generated from the dimensionless groups to test the effect of independently changing each variable in Eq. (5) above. Eleven test cases were developed; these are summarized in Table 2. The case for a 9.525 mm tube with $Re = 25,000$, $\beta = 0.185$, $\gamma = 0.2$ and $We = 805$ was chosen as the "basic case." With the basic case as a reference, one parameter was changed at a time to determine its influence on the drift velocity. It should be noted that when liquid velocity is changed, both Reynolds and Weber numbers are affected. A total of 11 numerical simulation tests were required to determine the influence of each individual parameter on the motion of a single bubble in a microgravity turbulent flow.

The test matrix chosen for this study allows practical two-phase flow conditions to be investigated. The Reynolds number for the numerical simulations covered a range from 11,000 to

Table 1
Dimensional analysis

Parameters	Dimensionless groups
$U, d, s, D, \rho_{\text{L}}, \mu_{\text{L}}, \sigma$	$V^+ = V_{\text{drift}}/U,\ \beta = s/D$ $\gamma = d/D,\ Re = DU\rho_{\text{L}}/\mu_{\text{L}}$ $We = DU^2\rho_{\text{L}}/\sigma$

Table 2
Summary of simulation parameters and drift velocity

Case notation	Simulation parameters	Simulation conditions	Maximum drift velocity, V^+_{max}
Test 1	$\beta = 0.185$, $D = 9.525$ mm, $We = 805$, $\gamma = 0.20$	$V_{SL} = 2.47$ m/s, $Re = 25,000$	0.0639
Test 2	$\beta = 0.185$, $D = 9.525$ mm, $We = 805$, $\gamma = 0.10$	$V_{SL} = 2.47$ m/s, $Re = 25,000$	0.0337
Test 3	$\beta = 0.185$, $D = 9.525$ mm, $We = 805$, $\gamma = 0.30$	$V_{SL} = 2.47$ m/s, $Re = 25,000$	0.0701
Test 4	$\beta = 0.235$, $D = 9.525$ mm, $We = 805$, $\gamma = 0.20$	$V_{SL} = 2.47$ m/s, $Re = 25,000$	0.0457
Test 5	$\beta = 0.286$, $D = 9.525$ mm, $We = 805$, $\gamma = 0.20$	$V_{SL} = 2.47$ m/s, $Re = 25,000$	0.0269
Test 6	$\beta = 0.185$, $D = 9.525$ mm, $We = 401$, $\gamma = 0.20$	$V_{SL} = 2.47$ m/s, $Re = 25,000$	0.0485
Test 7	$\beta = 0.185$, $D = 9.525$ mm, $We = 268$, $\gamma = 0.20$	$V_{SL} = 2.47$ m/s, $Re = 25,000$	0.0415
Test 8	$\beta = 0.185$, $D = 9.525$ mm, $We = 419$, $\gamma = 0.20$	$V_{SL} = 1.78$ m/s, $Re = 18,000$	0.0505
Test 9	$\beta = 0.185$, $D = 9.525$ mm, $We = 155$, $\gamma = 0.20$	$V_{SL} = 1.09$ m/s, $Re = 11,000$	0.0337
Test 10	$\beta = 0.185$, $D = 40.0$ mm, $We = 215$, $\gamma = 0.20$	$V_{SL} = 2.47$ m/s, $Re = 25,000$	0.0423
Test 11	$\beta = 0.185$, $D = 25.0$ mm, $We = 364$, $\gamma = 0.20$	$V_{SL} = 2.47$ m/s, $Re = 25,000$	0.0208

25,000. In contrast, most drift velocity models, by mathematical necessity, were only derived for creeping flows. The bubble sizes, relative to the tube diameters, covered a range from 0.1 to 0.3, where previous correlations assumed that the bubbles were far smaller than the tube diameter. In addition, large deformable bubbles introduce the effects of surface tension on the motion of the bubble. The surface tension itself varied from 7.28×10^{-2} N/m (for water) to 2.18×10^{-2} N/m, giving a Weber number in the range of 155–805. The tube diameter was varied from 9.525 to 40 mm, which corresponds to the available microgravity experimental data range of tube sizes.

4. Simulation

4.1. Numerical simulation

The CFD software FLUENT© (Release 4.4, 1996) was used to simulate the motion of a single bubble in a liquid flow through a tube of a circular cross-section. This version included the VOF computational method developed by Hirt and Nichols (1981). This method simulates multiphase flows with a defined interface between the two phases. The VOF model has a single set of momentum equations shared by the two fluids, and the volume fraction of each phase is recorded throughout the solution domain. It includes the surface tension model of Brackbill et al. (1992).

Turbulence is introduced by the conventional k–ε model with the standard wall function in the near wall region.

It was necessary to determine the suitability of the numerical code in solving two-phase flows involving a moving interface. A deformable air bubble rising from an initial condition of rest in a liquid reservoir to its final terminal velocity was chosen as the benchmark problem. The simulated bubble compared well to experimental data by Grace (1973); more details on this benchmark simulation are given in Clarke (1999).

The simulation of a bubble moving transverse by the liquid flow direction in a tube is more complicated than the case used in the benchmark problem. The problem is, by definition, three-dimensional, but processing time makes it difficult to solve it in a reasonable amount of time. Like early solutions of the bubble rise velocity in a stagnant liquid, the two-dimensional approximation was used.

4.2. Simulation set-up

The simulation of a single bubble moving in a turbulent liquid flow in microgravity requires several assumptions to be made. These are:

1. No significant mass or heat transfer across the bubble interface.
2. The inertial and viscous forces within the gas bubble are assumed to be negligible due to the large difference in density and viscosity between air and water.
3. The surface tension around the surface of the bubble is assumed to be constant.
4. The bubble is approximated as a two-dimensional object.

The last assumption is particularly important when interpreting the results of the bubble simulation. What is actually being simulated in a two- dimensional case is a cylindrical bubble moving in an infinite channel. This means that three-dimensional effects, such as those caused by the curvature of the tube surface and the bubble's surface, will not be accounted for in the simulation. This is significant, especially in cases where large bubbles exist very close to the tube wall (such is the case in this study). As well, the surface tension effects are reduced to a single curvature radius, and therefore the pressure difference across the bubble interface is reduced in the two- dimensional approximation. Physical properties of the liquid phase used in the simulation were chosen for a temperature of 20°C and at normal atmospheric pressure. This relates well to the conditions experienced during most of the microgravity experiments used later for comparison.

To limit the computer requirements of the solution, the bubble was chosen as the frame of reference, while the liquid velocities were defined in terms of their relative motion with respect to the bubble. This allows for a much shorter length of domain to be simulated and thus a faster solution. Previous results of numerical simulations of bubble motion in a tube were reported earlier by Tomiyama et al. (1995), who showed that reasonable results could be produced with a bubble as small as 6 cells in diameter. Our own simulations showed the behavior of bubbles simulated using 18 cells, 12 cells, and 6 cells had similar velocity, shape, and motion. Therefore a domain of 30 by 120 cells provided a good balance between simulation domain size and acceptable solution time.

Boundary conditions were chosen such that the inlet boundary has a fixed velocity profile typical of that for a turbulent flow. The initial shape of the liquid velocity profile at the inlet is modeled after the two-phase liquid velocity data reported by Kamp et al. (1993). This initial

velocity profile is copied across the entire domain so that the liquid within the domain is assumed to be already in motion at $t = 0$. The liquid is allowed to enter and exit the outlet as needed. Only half of the channel is modeled since axial symmetry about the centerline were substantiated during initial trials. A no-slip boundary condition was assumed at the wall. The wall was also assumed to be moving with the same velocity as the liquid adjacent to it because of the bubble being the reference frame.

With the initial conditions set arbitrarily for a specific liquid velocity profile across the channel and a spherical bubble placed in the flow, simulations were performed for this "artificial" condition. This is especially true near the bubble where the solution must eventually evolve into the proper pressure distribution and velocity profile once the simulation started. Therefore data from the early part of the simulation (as the bubble undergoes its initial deformation into an elongated shape before it starts moving away from the wall towards the tube's center), must be treated with caution. Finally, the convergence and residual limits for each time-step of the solution were set to 0.00001.

4.3. Typical simulated bubble

A general discussion of the behavior of individual bubbles as each dependent parameter is changed is valuable in predicting the bubble motion under a variety of flow situations. Generally, all simulation results have the same basic characteristics with the only change being the magnitude of forces acting on the bubble. Hence, a single simulation was chosen to view, in some detail, the mechanism of drift velocity. Referring back to Table 2, the simulation chosen for detailed discussion was Test 8 ($\beta = 0.185$, $D = 9.525$ mm, $Re = 18000$, $We = 419$, $\gamma = 0.20$).

The simulation results of the evolution of the shape of the bubble as it moves from its initial position to its final position close to the centerline is shown in Fig. 6(a). The bubble

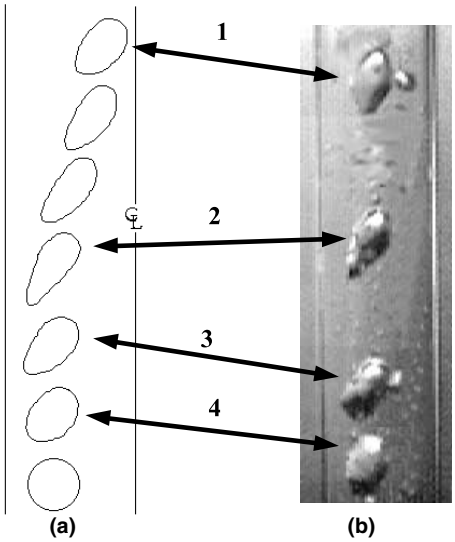

Fig. 6. Bubble sequences for bubble at $Re = 18,000$; (a) Simulation, and (b) Experimental.

starts with an initially spherical shape in the liquid flow field and immediately starts to elongate as the liquid velocity gradient acts to "stretch" the bubble. This "stretching" of the bubble continues until a balance is reached between the liquid forces acting upon the bubble interface and the surface tension of the bubble. Because of the higher liquid velocity gradient acting on the wall-side of the bubble, a "tail" of gas is pulled towards the wall which tends to cause a very small initial drift velocity towards the wall. Once the bubble elongates, it then starts to move quickly towards the centerline and out of the region of high liquid shear to lower shear. As the tail of the bubble exits the high shear area, it is pulled back into the bubble forming a more ovaloid shape. The shape of the bubble continues to return to a nearly spherical shape as it approaches the centerline, and the drift velocity of the bubble steadily decreases. The liquid shear acting on the bubble continues to decline and a critical value of the velocity gradient is arrived at where the bubble will no longer continue traveling towards the center. Notice that the bubble does not return entirely to its initial spherical shape because it is still subjected to a low shear. Comparing the simulation to a typical bubble from the experimental data in Fig. 6(b) shows the similarity between them at various points in their motion towards the center of the tube.

Examining the liquid velocity field around the bubble as it moves towards the centerline illustrates the bubble evolution at different stages. Fig. 7(a) shows the simulation at $t = 0.02$ s. This is the point at which the bubble is moving towards the center with a maximum velocity. The liquid velocity vectors are relative to the bubble velocity at $t = 0$ s (initial bubble position), and hence clearly show the relative motion between the bubble and the liquid. The liquid on the wall-side of the bubble is moving upstream (with respect to the bubble), while on the core-side of the bubble it is moving downstream.

Referring back to the interface equations (3) and (4) helps us to explain the shape of the bubble as it moves towards the center with the balance between the shear and surface tension forces. Recalling the interface boundary conditions for a gas bubble in a liquid, a tangential stress is applied to the bubble surface due to the viscous force of the fluid moving around the bubble, and is considered to be the primary reason for the bubble's elongation. This perhaps can be seen in Fig. 7(a), where the liquid velocity vectors are pointed towards the ends of the bubble, resulting in viscous stresses that elongate the bubble in the direction of the liquid velocity vectors. The normal stress boundary condition shows that the pressure field in the liquid around the bubble is balanced by the pressure inside the bubble and the surface tension forces. Thus, there exists two competing forces acting on the bubble surface, the liquid flow which acts to deform the bubble and the surface tension acting to retain the bubble's spherical shape.

Fig. 7(c) shows the bubble at $t = 0.04$, prior to reaching its final position. A comparison of the bubble at $t = 0.02$ and 0.04 illustrates the influence of the liquid velocity field around the bubble and the balance between the liquid shear and surface tension. The first difference is in the shape of the bubble as it is returning to a more spherical shape at $t = 0.04$. The velocity field around the bubble has also changed as seen by comparing Figs. 7(a) and (c). The bubble at $t = 0.04$ moves faster in the downstream direction than it did at $t = 0.02$, as it moves into a higher liquid velocity region near the centerline. The liquid velocity difference across the width of the bubble at $t = 0.04$ is much smaller with correspondingly less circulation around the bubble. Lower liquid velocities near the bubble act to reduce the effect of viscous forces at the interface, and hence surface tension acts to return the bubble to a nearly spherical shape.

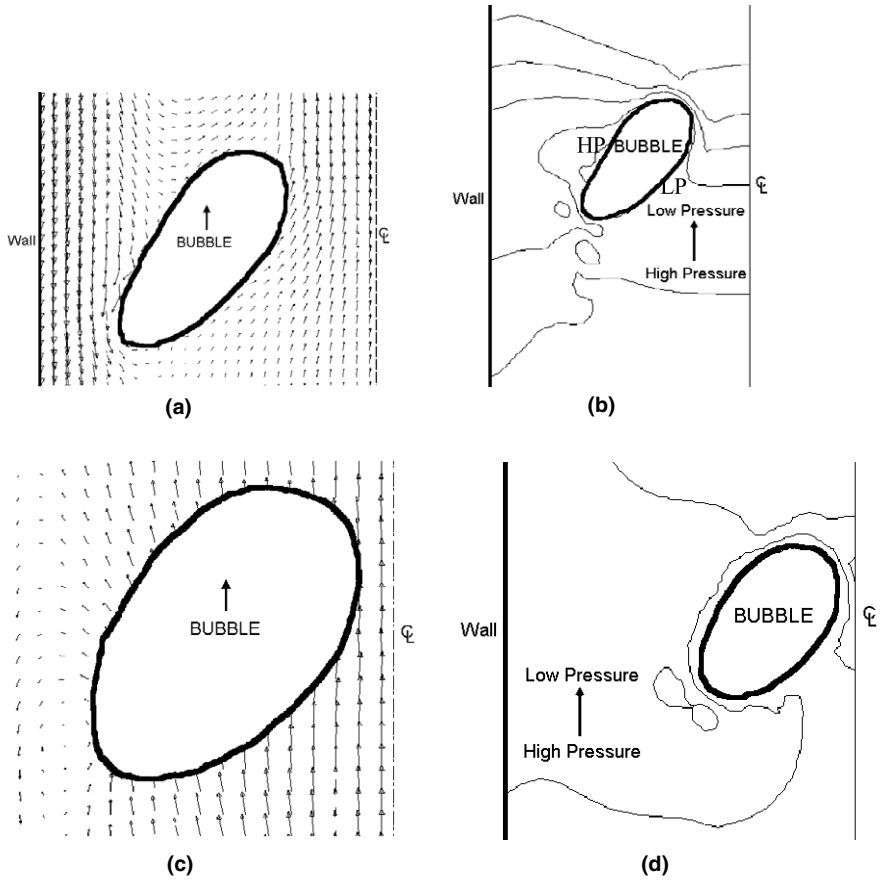

Fig. 7. Liquid velocity and pressure fields for test 8; (a) velocity field at $t = 0.02$ s, (b) pressure field at $t = 0.02$ s, (c) velocity field at $t = 0.04$ s, and (d) pressure field at $t = 0.04$ s.

From the previous discussion it can be concluded that the shape of the bubble plays a significant role in its motion towards the center of the tube in μ-g liquid flows. The motion of the bubble is due to the liquid circulation and associated pressure field around the elongated bubble. The pressure distribution around a bubble helps to explain how the mechanism of motion operates. Fig. 7(b) shows the pressure contours around the bubble in Test 8 (at $t = 0.02$), where the bubble is moving at maximum velocity towards the centerline.

As previously discussed, the bubble elongates into what can be termed as a ''wing-shape''. This analogy is useful in describing the flow of liquid around the bubble and possibly the cause for the motion of the bubble towards the centerline. Consider an airfoil in a steady velocity field of moving air. Discarding gravity terms, the balance of static and kinetic pressure between any two points around the airfoil can be obtained from Bernoulli's equation. According to Bernoulli's principle, a high fluid velocity is accompanied by a low-pressure region. For the airfoil, the fluid accelerates over the top of the foil creating a low-pressure region that results in lift. The liquid flow around an elongated bubble follows, more or less, the same trend as an airfoil. Where the

relative liquid velocity around a bubble is high, a low-pressure zone will form and a net force on the bubble surface will be realized.

The net force acting on the bubble can be divided into two components; a drag (stream-wise component) and lift force (radial component). The lift force component is what forces a bubble to move radially towards the channel's wall or centerline. Distinct low-pressure and high-pressure zones around the bubble are demonstrated in Fig. 7(b). There is a high-pressure region on the wall-side of the bubble and a low-pressure zone on the core- side of the bubble. This pressure difference creates a net lift force acting towards the center of the channel. The velocity vectors in Fig. 7(a) clearly shows the source of the low-pressure and high-pressure zones. On the wall-side there is a large area of little or no liquid motion (high-pressure), where surface flow along the interface stagnates. On the core-side there is a comparatively high velocity (low-pressure) region on the core-side.

As the bubble approaches the centerline at $t = 0.04$, the pressure field significantly changes; this is demonstrated in Fig. 7(d). The magnitude of the pressure differences around the surface of the bubble is greatly decreased, and this results in a much smaller lift force acting on the bubble. The bubble is moving at only a fraction of the velocity that it had at $t = 0.02$, which is also seen to support the results from the pressure distribution around the bubble.

5. Comparison with experimental data

The results from the numerical simulation were compared to the video image data reported by Lowe and Rezkallah (1999) in a 9.525 mm diameter tube. The recorded images were taken during microgravity testing aboard the NASA DC-9 zero gravity aircraft. The simulation bubble and an experimental bubble at $Re = 18,000$ were shown earlier in Fig. 6. The bubble deformation towards the centerline can be clearly seen in both cases. Moreover, the video images also show that the bubbles appear to move towards the center and return to a more spherical shape once they reach the core area. The somewhat exaggerated magnitude of the bubble elongation seen in the simulation could be attributed to the simulation being two- dimensional. As well, the interaction between the bubble and the surrounding bubbles (not shown in the figure to avoid clutter), and the presence of a wake region in the actual motion could have also contributed to the differences.

A quantitative comparison between the simulation and experimental results is done by comparing the maximum dimensionless drift velocity (V^+_{max}) of both the experimental and simulated bubbles. The experimental data have liquid velocities as follows: $V_{SL} = 0.74$, $V_{SL} = 1.78$, and $V_{SL} = 2.53$ m/s (which correspond to liquid Reynolds numbers of 7900, 18,000 and 25,500, respectively). These values compare well with the simulation Reynolds numbers of 11,000, 18,000 and 25,000. It is important to remember that for observations in the recorded images, the bubbles appear on the screen for a short period (less than 0.10 s), and that the size of the bubbles was small compared to the pixel resolution of the images. This provides for only a few data points (4–5) that can be collected for each bubble trace. The error in the recorded position was based on a measurement error of one pixel and for a 40 pixel measurement would equal ±2.5% (depending upon the length being measured).

Table 3 summarizes the comparison of the experimental to simulation data for the three Reynolds numbers of 11,000, 18,000 and 25,000. The drift velocity was calculated by dividing

Table 3
Comparison of experimental and simulation data

Case	V^+_{max}		Time to center (s)		Distance moved (s/D)	
	Simulation	Experimental	Simulation	Experimental	Simulation	Experimental
$Re = 11,000$	0.034	0.049	0.084 s	0.044 s	0.100	0.080
$Re = 18,000$	0.051	0.054	0.032 s	0.019 s	0.194	0.063
$Re = 25,000$	0.057	0.064	0.024 s	0.011 s	0.172	0.090

the difference in position of the bubble from one time increment to the next by the time increment. Comparing the values of maximum velocity shows that they are similar with a difference of 12% for the 18,000 and 25,000 cases but the difference was much larger in the 11,000 case. The larger difference in the latter case can be attributed to the much larger bubble in the experimental data, which in turn would greatly increase its velocity towards the tube center. The time that it took for the bubbles to move to a position in the center of the tube are also similar. In all cases it took the experimental bubbles less time, but it is impossible to tell whether they had reached their final position because the bubbles stayed in the viewing area for such short times. In fact, comparing the radial distance that the bubbles moved, it is possible to suppose that the experimental bubbles do not complete their motion to the center while they are still visible in the viewing area. In all cases the simulation bubble moved farther distances, and took more time to reach the center of the tube. Therefore the most important evidence that the simulation adequately models the drift velocity phenomenon is the velocity data that shows similar maximum velocities. Any differences between the two can be attributed to differences between the experimental and simulation conditions. In actual flow the bubble's motion could be influenced by interaction with other bubbles, or the presence of a wake region from preceding bubbles. It can thus be said that the general trends of motion, bubble shape, bubble evolution, and time scale were very comparable to those obtained from the simulation results.

6. Parametric study results

In the following section, we discuss the results from the parametric study using the test matrix of Table 2. The examined parameters were the bubble size, bubble starting position, surface tension effects, liquid Reynolds number and tube size. These will be discussed separately in the following section.

6.1. Bubble size

The effect of changing the bubble size on the drift velocity is shown graphically in Fig. 8 where all other parameters were held constant. The results are shown for three bubble-to-diameter ratios ranging from 0.1 to 0.3. The bubbles all start at a common initial position and move towards the centerline and stop their motion at a point away from the centerline. The slope of the lines in Fig. 8

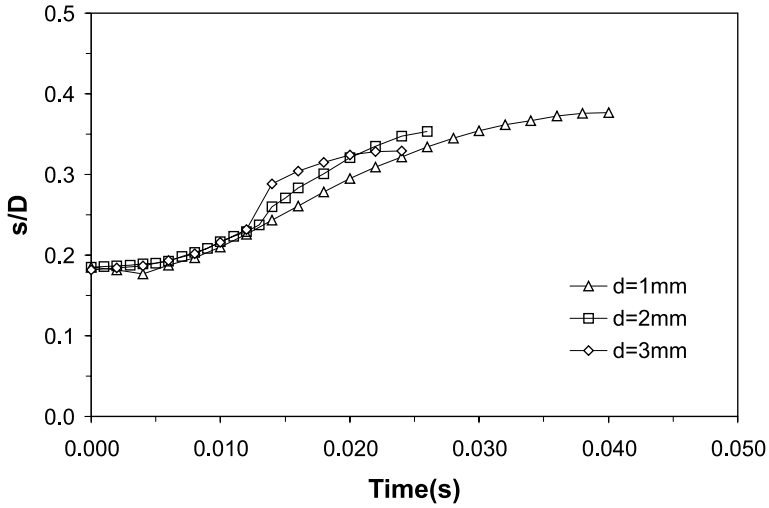

Fig. 8. Effect of bubble size on bubble position as a function of time.

Test	$\gamma\ (=d/D)$	$V^{+}_{\max}$
2	0.1	0.0337
1	0.2	0.0639
3	0.3	0.0701

equals to the bubble velocity. As seen from the results summarized below the figure, the larger the bubble, the greater is the drift velocity. The evolution of the bubble and its drift velocity can be characterized by an initial period in which the bubble is elongating and accelerating in the liquid shear flow. The bubble will then reach a maximum velocity at which point it decelerates and, as it continues to move towards the centerline, it will eventually stop. This is due to the liquid shear around the bubble decreasing to the point where it is no longer adequate to move the bubble to the centerline. As the bubble decelerates, it also returns to a more spherical shape (as the liquid shear acting to elongate the bubble is reduced).

6.2. Bubble starting position

The location at which the bubble is initially placed in the flow has some influence on its motion. Fig. 9 shows the path of a bubble to its final position near the centerline for three initial starting positions with each bubble starting progressively closer to the centerline (and hence in regions of progressively less shear). All three bubbles end their motion at the same distance from the centerline ($s/D = 0.35$), and they reach different maximum drift velocities. Considering the estimated drift velocity values shown in Fig. 9, it is clear that the bubble starting at $\beta = 0.185$ attains the highest drift velocity. This is expected since in this case, the bubble starts in a region of higher liquid velocity gradients compared to the other two cases.

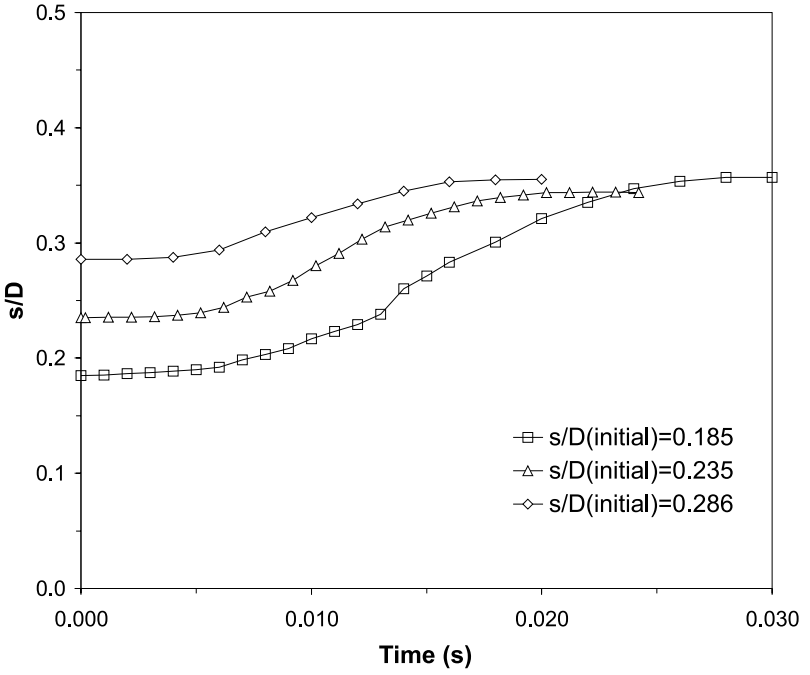

Fig. 9. Effect of initial bubble position on bubble position as a function of time.

Test	$\beta\ (=s/D)$	$V^{+}_{\max}$
1	0.185	0.0639
4	0.235	0.0457
3	0.286	0.0269

6.3. Surface tension

The effect of changing the liquid Weber number (by changing the surface tension) on the drift velocity can be demonstrated from the results shown in Fig. 10. A cursory observation of the results may indicate conflicting trends. The high Weber number ($We = 805$), and thus low surface tension bubble, does not seem to move any faster towards the centerline than the bubble associated with $We = 401$, while the bubble with $We = 268$ has a slightly lower drift velocity. Considering the maximum drift velocity for the three Weber numbers, it can be seen that the $We = 805$ bubble has a higher maximum drift velocity than the $We = 401$ bubble. Hence, it could be concluded that lower surface tension results in higher drift velocity. The drift velocity depends on the surface tension to a lesser extent than seen previously with the bubble size. Generally, the drift velocity appears to be closely related to the extent to which the bubble elongates as it moves towards the tube center. Less elongation (which in this case is due to high surface tension) gives a lower drift velocity.

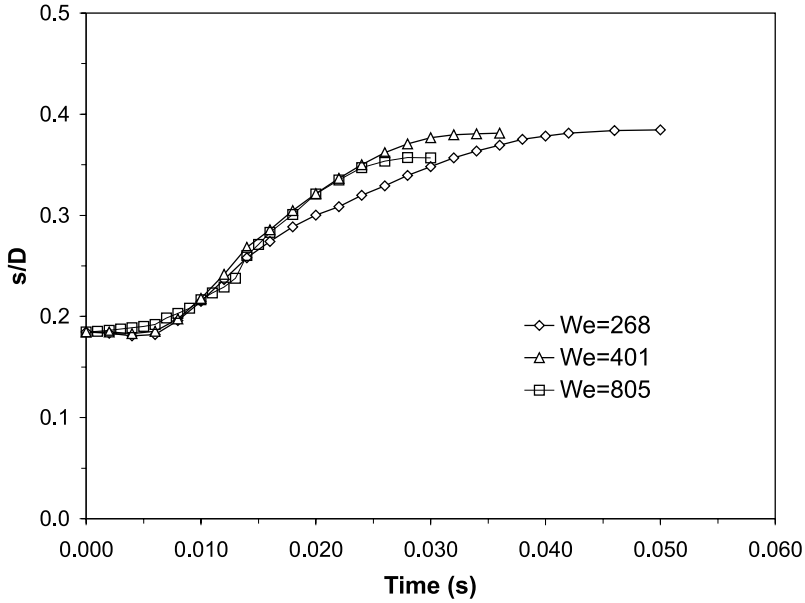

Fig. 10. Effect of surface tension on bubble position as a function of time.

Test	We	V^{+}_{max}
1	805	0.0639
6	401	0.0485
7	268	0.0415

6.4. Liquid Reynolds number

The results due to increasing the liquid Reynolds number (through increasing the liquid velocity) are shown in Fig. 11. It should be noted that as the Reynolds number increased, the Weber number increased to a larger proportion due to the power that appears on the velocity term in the Weber number. The bubble traces for all three Reynolds numbers in the turbulent flow regime show that the drift velocity always increases with increasing the Reynolds number. This is clearly shown in the numerical data below the figure. The Reynolds number appears to also influence the distance from the centerline to which the bubble penetrates. This could be attributed to the effect of a minimum liquid velocity difference across the bubble that is required to produce motion.

6.5. Tube diameter

Among all the parameters examined in this study, it was found that the tube diameter has the most profound influence on the magnitudes and trends of the bubble drift velocity. This can be clearly demonstrated from the results shown in Fig. 12. The simulation results show that as the diameter increases, the drift velocity decreases for the same liquid Reynolds number. While all three flows have the same liquid Reynolds number, referring to the equation for Reynolds number

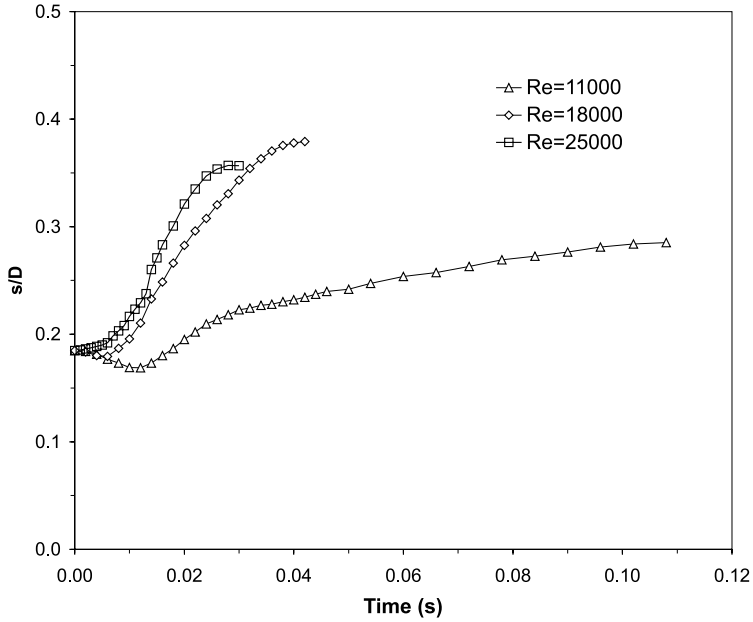

Fig. 11. Effect of Reynolds number on bubble position as a function of time.

Test	*Re*	V^{+}_{max}
9	11,000	0.0337
8	18,000	0.0505
1	25,000	0.0639

shows that the liquid velocity decreases as the tube diameter increases. This supports the results of the previous section on the effect of the liquid velocity, where the drift velocity decreases with decreasing the liquid velocity.

7. Conclusions

This paper presented a numerical simulation of the motion of a dispersed bubble in a liquid flow under microgravity conditions. The simulation focussed on individual gas bubbles in a two-dimensional flow, and the rate at which the bubbles move towards the tube center (the drift velocity). Dimensional analysis determined the significant flow parameters to be the bubble size, surface tension, liquid velocity, tube diameter, and the radial bubble position.

The drift velocity simulations were completed for 11 tests to cover the parameters deemed significant from a dimensional analysis. The liquid Reynolds number was varied from 11,000 to 25,000. The bubble size relative to the tube diameter ranged from 0.1 to 0.3. The surface tension varied from 7.28×10^{-2} to 2.18×10^{-1} N/m; corresponding to a change in the liquid Weber number from 155 to 805. The tube diameter was varied from 9.525 to 40 mm. The shape

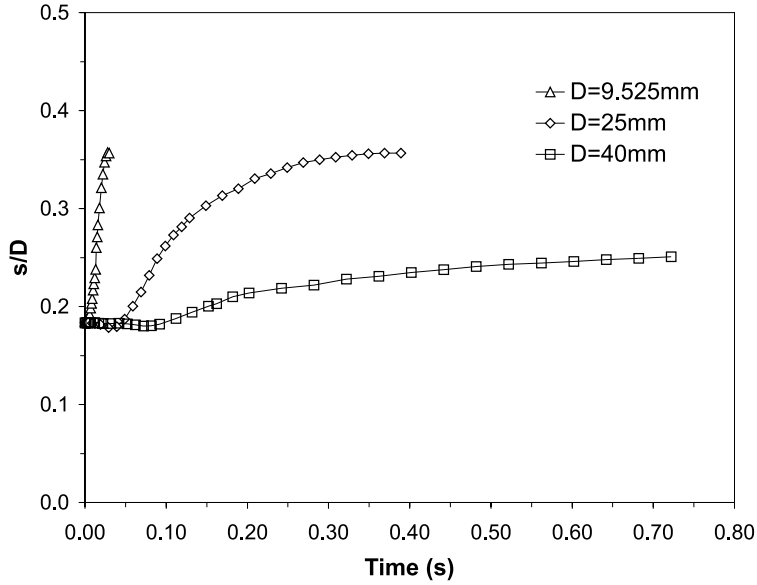

Fig. 12. Effect of tube diameter on bubble position as a function of time.

Test	D	V^{+}_{max}
1	9.525	0.0639
11	25	0.0423
10	40	0.0208

evolution, motion, and drift velocity of the simulated bubbles were compared to the experimental data collected during actual microgravity testing aboard NASA's DC-9 zero gravity aircraft.

The motion of liquid around a bubble causes it to elongate into an elliptical shape as it moves towards the tube center. Consequently, the elliptical shape changes the flow of the liquid around the bubble and hence the pressure field around the bubble. Integrating the pressure around the bubble surface produces a net force acting on the bubble. The radial component is the lift force that moves the bubble towards the tube centerline.

The following conclusions can be drawn from the numerical bubble simulation:

- Comparison of the simulation results with previous experiments showed the same tendency in bubble shape and evolution, drift velocity magnitude, and the distance that the bubble moves radially towards the tube center.
- The bubble drift velocity is dependent upon the magnitude of the bubble's elongation into an elliptical cross-sectional shape. The amount of elongation is a result of the balance of forces acting on the bubble. Liquid circulation around the bubble tends to stretch the bubble towards the tube center, while the surface tension acts against the liquid viscous force to maintain a spherical shape. A more extreme bubble distortion alters the pressure distribution around the bubble and increases the drift velocity.

- Larger bubbles ($d/D > 0.1$) were found to elongate more than smaller bubbles and results in higher drift velocities.
- Bubbles, initially closer to the wall, experience higher liquid velocity gradients which cause higher drift velocities and more elongation.
- Bubbles in higher Reynolds number flows experience larger liquid velocity gradients and hence higher drift velocities.
- Bubbles in larger tubes ($D > 10$ mm) experience less liquid shear, elongate less, and have correspondingly lower drift velocities.
- Increases in surface tension also result in lower drift velocity and less bubble elongation.

The present study discarded several factors that were beyond the resources available for the computer simulation of bubbly two-phase flow. In particular future studies that use a three-dimensional bubble simulation would eliminate any two-dimensional phenomenon seen in the results presented here. As well, experiments dealing with individual bubbles moving in microgravity two-phase flow would be useful to verify bubble simulations directly.

Acknowledgements

The authors want to acknowledge the financial support from the Natural Science and Engineering Research Council (NSERC).

References

Antal, S.P., Lahey, R.T., Flaherty Jr., J.E., 1991. Analysis of phase distribution in fully developed laminar bubbly two-phase flow. Int. J. Multiphase Flow 17, 635–652.

Brackbill, J.U., Kothe, D.B., Zemach, C., 1992. A continuum method for modeling surface tension. J. Comput. Phys. 100, 335–354.

Clarke, N.N., 1999. A study of the drift velocity in bubbly two-phase flow under microgravity conditions. M.S. Thesis, University of Saskatchewan, Saskatoon, Canada.

Cox, R.G., Hsu, S.K., 1977. The lateral migration of solid particles in a laminar flow near a plane. Int. J. Multiphase Flow 3, 201–222.

Drew, D.A., Lahey Jr., R.T., 1982. Phase-distribution mechanisms in turbulent low-quality two-phase flow in a circular pipe. J. Fluid Mech. 117, 91–106.

Drew, D.A., Lahey Jr., R.T., 1987. The virtual mass and lift force on a sphere in rotating and straining inviscid flow. Int. J. Multiphase Flow 13, 113–121.

Fluent Incorporated, 1996. FLUENT User's Guide Release 4.4.

Hirt, C.W., Nichols, B.D., 1981. Volume of fluid (VOF) method for the dynamics of free boundaries. J. Comput. Phys. 39, 201–225.

Grace, J.R., 1973. Shapes and velocities of bubbles rising in infinite liquids. Trans. Inst. Chem. Engrs. 51, 116–120.

Ishii, M., 1975. Thermo-fluid Dynamic Theory of Two-Phase Flow. Eryolles, Paris.

Kamp, A., Colin, C., Fabre, J., 1993. Bubbly flow in a pipe: influence of gravity upon void and velocity distributions. In: 3rd World Conference on Experimental Heat Transfer, Fluid Mechanics and Thermodynamics, Honolulu, Hawaii.

Lahey Jr, R.T., Bonetto, F., 1994. Analysis of phase distribution phenomena in microgravity environments. In: Second Microgravity Fluid Physics Conference, Cleveland, OH, June 21–23.

Lin, Y., Rezkallah, K.S., 1995. Numerical predictions of turbulence structure in gas–liquid bubbly flows under normal and micro-gravity conditions. In: Proceedings of the Second International Conference on Multiphase Flow, Kyoto, Japan.

Lowe, D., Rezkallah, K.S., 1999. Flow regime identification in microgravity two-phase flows using void fraction signals. Int. J. Multiphase Flows 25, 433–457.

Rezkallah, K.S., Nakazawa., 1998. A study of the slip ratio in two-phase gas-liquid flow at normal and microgravity conditions. In: Proceedings of 1998 ASME Fluids Engineering Division Annual Summer Meeting.

Saffman, P.G., 1965. The lift on a small sphere in a slow shear flow. J. Fluid Mech. 22, 385–400.

Saffman, P.G., 1968. Corrigendum. J. Fluid Mech. 31, 624.

Serizawa, A., Kataoka, I., Michiyoshi, I., 1975. Turbulence structure of air–water bubbly flow-II. Local properties. Int. J. Multiphase Flow 2, 235–246.

Singhal, M., Bonetto, F.J., Lahey Jr., R.T., 1996. Phase distribution phenomena for simulated microgravity conditions: experimental work. In: Proceedings of the Third Microgravity Fluid Physics Conference.

Tomiyama, A., Suo, A., Zun, I., Kanami, N., Sakaguchi, T., 1995. Effects of Eotvos number and dimensionless liquid volumetric flux on lateral motion of a bubble in a laminar duct flow. In: Proceedings of the 2nd International Conference on Multiphase Flow, Kyoto, Japan.

Wang, S.K., Lee, S.J., Jones Jr., O.C., Lahey Jr., R.T., 1987. 3-D turbulence structure and phase distribution measurements in bubbly two-phase flows. Int. J. Multiphase Flow 3, 327–343.